Particle capture in a model chaotic flow

Mengying Wang [1], Julio M. Ottino [1,2,3] Richard M. Lueptow [1,2,3] and Paul B. Umbanhowar [1,*]
[1]*Department of Mechanical Engineering, Northwestern University, Evanston, Illinois 60208, USA*
[2]*Department of Chemical and Biological Engineering, Northwestern University, Evanston, Illinois 60208, USA*
[3]*Northwestern Institute on Complex Systems (NICO), Northwestern University, Evanston, Illinois 60208, USA*

(Received 4 June 2021; accepted 8 November 2021; published 6 December 2021)

To better understand and optimize the capture of passive scalars (particles, pollutants, greenhouse gases, etc.) in complex geophysical flows, we study capture in the simpler, but still chaotic, time-dependent double-gyre flow model. For a range of model parameters, the domain of the double-gyre flow consists of a chaotic region, characterized by rapid mixing, interspersed with nonmixing islands in which particle trajectories are regular. Capture units placed within the domain remove all particles that cross their perimeters without altering the velocity field. To predict the capture capability of a unit at an arbitrary location, we characterize the trajectories of a uniformly seeded ensemble of particles as chaotic or nonchaotic, and then use them to determine the spatially resolved fraction of time that the flow is chaotic. With this information, we can predict where to best place units for maximum capture. We also examine the time dependence of the capture process, and demonstrate that there can be a trade-off between the amount of material captured and the capture rate.

DOI: 10.1103/PhysRevE.104.064203

I. INTRODUCTION

Many processes are possible within the fabric of a chaotic flow. Fluid droplets can break and disperse [1], particles can agglomerate [2], clusters can fragment [3], autocatalytic reactions can be enhanced [4], and floating matter can accumulate in specific regions of the flow [5]. And in chaotic granular flows, in a surprising parallel, initially well-mixed grains may demix, with certain particles, denser or smaller, accumulating in regular regions of the flow [6,7]. Here we consider the flow capture problem, which focuses on removing passive scalars from a fluid flow. Practical applications include removing pollutants circulated by geophysical flows, which is a topic of global importance with, arguably, the most pressing application being the removal of greenhouse gases from the atmosphere [8–10]. This is due to the fact that the atmospheric concentration of CO_2 due to human activity has risen dramatically in the last few decades [11] with associated consequences including increases in sea level and global mean temperature. Some of the measures to reduce climate change include chemically absorbing greenhouse gases actively removed from the atmosphere, developing carbon-neutral fuels, and growing more plants [12].

For the most efficient and rapid active removal of greenhouse gases, a better and more principled understanding of where to best site CO_2 removal units is required. Similar understanding is also needed to most effectively remove plastic debris from the ocean [13–15]. However, one of the challenges of solving the flow capture problem is the complex spatiotemporal variation of flows in the atmosphere and the ocean. The work described here extends the work of Smith *et al.* [16], who studied the dependence of capture unit efficiency on position in a chaotic flow field, to develop a deeper understanding of how flow structure influences capture efficiency.

Several studies have considered transport in geophysical flows. For example, Lekien *et al.* [17] modeled the spread of passive drifters off the coast of Florida using measured ocean velocity data. Tallapragada *et al.* [18] studied the advection of microorganisms in the atmosphere to inform systems for pest control and disease management. Nolan *et al.* [19,20] measured the local atmospheric flow field to predict the spread of airborne chemicals. Schmale and Ross [21] studied the atmospheric transport of plant pathogens from the pathogen scale to the continental scale. All these studies predict material transport but lack a standard means of characterizing the relevant properties of the chaotic flow field.

In order to avoid the complexity of real geophysical flows while focusing on fundamental aspects of the flow capture problem, we study a model chaotic flow, specifically the two-dimensional double-gyre model [22], which exhibits similar dynamical properties to real geophysical flows [23,24]. In particular, geostrophic flows commonly have features that limit transport in and out of isolated regions. These "barriers to transport" can arise due to geographical features, e.g., mountains and valleys, or flow structures such as vortices. For example, the Florida Current displays complex vortical patterns [25], the Santa Barbara Channel has cyclonic and anticyclonic vortices which propagate with an average period of two weeks [26], and ocean current patterns in Monterey Bay include coherent and nonlinear structures [27].

Analogous barriers to transport occur in model chaotic flows, both autonomous and nonautonomous. In autonomous (time-independent) flows, fixed points (zero velocity points) of the governing ordinary differential equations (ODEs) are critical for determining the barriers to transport [28,29]. The

*Corresponding author: umbanhowar@northwestern.edu

fixed points are either elliptic, hyperbolic, or parabolic depending on the eigenvalues of the Jacobian at the fixed points [30]. Barriers to transport always lie between hyperbolic points where both stretching and compression occur, thereby separating various regions of the flow [31,32]. The situation is more complicated in nonautonomous (time-dependent) flows. Because zero velocity points in the flow typically move, barriers to mixing also move and change shape as well. For the problem of fixed capture units in a time-dependent chaotic flow that we consider here, the movement of barriers to mixing with respect to the capture unit can significantly impact the effectiveness of the capture unit.

In this paper, we use the double-gyre flow to study how the structure of a time-dependent chaotic flow determines optimal capture unit placement. We follow the approach of Smith *et al.* [16] by advecting tracer particles (passive scalars) in the double-gyre flow for a range of flow parameters and then removing tracers from the flow when their trajectories intersect the perimeter of a capture unit. Here we show how the overall flow structure and the fraction of chaotic trajectories passing through a capture unit influence its effectiveness. Perhaps just as importantly, we introduce a numerical technique connecting the Lagrangian and Eulerian frameworks by combining aspects of Poincaré maps and Lyapunov exponents.

This paper is organized as follows. After introducing the double-gyre flow model in Sec. II, we describe tools to characterize the nature of the flow and particle capture in Sec. III. Then we present an algorithm to detect and characterize structures in nonautonomous flows in order to predict the potential of flow capture units based on their location with respect to transport barriers in Sec. IV. Next we discuss how capture unit placement relative to flow structures affects the degree of tracer particle capture in Sec. V. In Sec. VI we discuss the particle capture rate and identify factors that influence it. Section VII presents conclusions and directions for future work.

II. A MODEL CHAOTIC GEOPHYSICAL FLOW

We use the double-gyre flow model to investigate the flow capture problem. The double-gyre flow is two-dimensional and time periodic and produces chaotic flows and barriers to transport with appropriate parameter choices. Its velocity field is given by

$$v_x(x, y, t) = -\pi A \sin[\pi f(x, t)] \cos(\pi y), \tag{1a}$$

$$v_y(x, y, t) = \pi A \cos[\pi f(x, t)] \sin(\pi y) \frac{\partial f}{\partial x}(x, t), \tag{1b}$$

$$f(x, t) = \epsilon \sin(\omega t) x^2 + [1 - 2\epsilon \sin(\omega t)] x, \tag{1c}$$

where A is a velocity amplitude, and ϵ and $\omega/2\pi$ control the amplitude and frequency of the temporal flow variation, respectively. We consider the flow in a 2×1 rectangular region, and fix $A = 0.5$ and $\omega = 2\pi$, while studying the dependence of flow capture on ϵ. The velocity field over a flow period is illustrated in Fig. 1 for $\epsilon = 0.25$. At $t = 0$ the flow consists of two symmetric vortices (gyres) separated by vertical line along which $v_x = 0$. For $t > 0$, the $v_x = 0$ line oscillates in the x-direction with right and left extremes occurring at $t = 0.25$ and $t = 0.75$, respectively. At $t = 0, 0.5, 1$, the separation line is located at $x = 1$. The parameter ϵ in Eq. (1c) determines the maximum x-displacement of the $v_x = 0$ line. At all times, the vortex on the left rotates clockwise and vice versa.

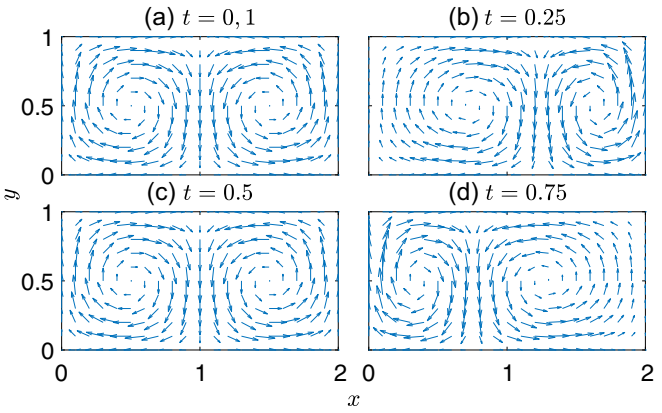

FIG. 1. Periodic time dependence of the velocity field of the double-gyre flow [Eq. (1)] with $\omega = 2\pi$, $A = 0.5$, $\epsilon = 0.25$.

The double-gyre flow shares similarities with real geophysical flows in that it exhibits periodic patterns and vortices that change position [22]. As such, the double-gyre flow is a useful model of real geophysical flow that is easier to study given its analytic form. Consequently, we focus on its dynamical properties to understand the fundamentals of the flow capture problem.

III. FLOW AND POLLUTANT CAPTURE CHARACTERIZATION

The Poincaré map is a useful tool to visualize transport in the double-gyre model. It is generated by calculating the trajectories of tracer particles (points) in the flow and plotting their positions after equal interval integer flow periods n [29]. In the Poincaré map, tracer particles initially located in nonchaotic flow regions form KAM islands [33–35] that become evident after many iterations of the map. Each island contains at least one elliptic point [31]. Tracer particles initially located in chaotic regions explore the entire "chaotic sea." Figures 2(a) and 2(b) show examples of Poincaré maps for two different ϵ. For $\epsilon = 0.01$, the two gyres move only slightly from side to side and most of the domain is nonchaotic, evident by the approximately circular structures in the Poincaré map. For larger ϵ ($\epsilon = 0.05$), the lateral displacement of the two gyres grows, resulting in a relatively large chaotic sea (regions of the Poincaré map with no evident structure) and smaller nonchaotic islands.

A crucial factor here is that because the double-gyre flow is time-dependent, the nonchaotic regions move and change shape within one flow period. With $\omega = 2\pi$, the flow period is 1, and a typical Poincaré map is generated based on the location of tracer particles at integer numbers of flow periods, n. However, the Poincaré map changes at other times during the cycle. To illustrate this dependence we consider the Poincaré map at different phases θ, *i.e.* at $t = n + \theta$, where $0 \leqslant \theta \leqslant 1$. To show the movement of nonchaotic islands in the Poincaré map at other phases, we consider the boundaries, outlined in

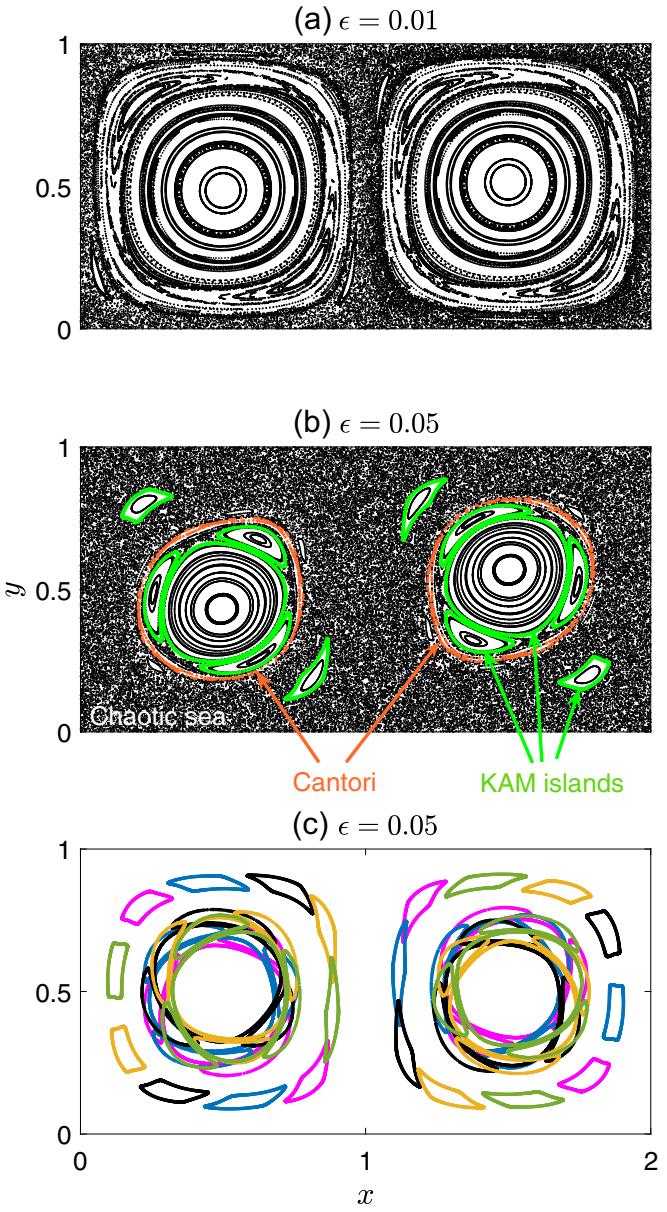

FIG. 2. Poincaré map of double-gyre flow with (a) $\epsilon = 0.01$ and (b) $\epsilon = 0.05$. Map is created by plotting the position of 200 tracer particles seeded uniformly across the domain for $n = 0, 1, 2, \ldots, 500$ periods of the map. In (b), boundaries between nonchaotic islands and the chaotic sea as well as two Cantori (see text) are indicated. (c) Island boundaries at different phases $\theta = 0, 0.2, 0.4, 0.6, 0.8$ of the flow period are indicated by different colors (gray scale intensities).

Fig. 2(b), between the main islands in each half of the domain and the chaotic sea, ignoring smaller nonchaotic islands. We plot the boundaries of these main islands extracted from the Poincaré map at four other phases $\theta = 0.2, 0.4, 0.6, 0.8$ in Fig. 2(c), where different colors (gray scale intensities) represent different phases. The resulting boundaries of the nonchaotic regions at all five phases form a ringlike structure surrounding a large central structure in each half of the domain. Filling in the regions between these period-2 islands by calculating the Poincaré map with finer phase resolution

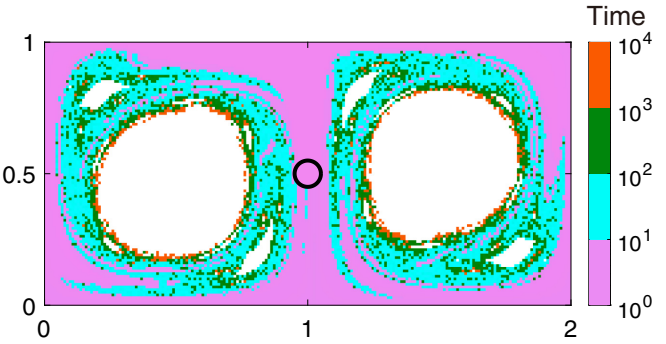

FIG. 3. Initial locations of a 100×200 grid of tracer particles captured by the capture unit [circle at (1, 0.5)] and colored (shaded) by the time interval in which they are captured. White regions indicate particles not captured in 10^4 periods. $\epsilon = 0.05$.

would create continuous rings surrounding the large nonchaotic regions indicating that the islands move continuously through the domain. We also note the existence of leaky barriers to mixing within the chaotic sea and surrounding the nonmixing islands, which are called Cantori [36], also called "ghost" tori [37], as labeled in Fig. 2(b). Cantori result from the breakup up of KAM tori and can be viewed as tori with fractal distributions of holes, similar to a Cantor set [37–39]. We return to the effects of Cantori on capture in Sec. V.

Smith *et al.* [16] noted that the Poincaré map gives hints to the capture capability of individual circular capture units at particular locations in the flow. A single capture unit placed so that it is always in the chaotic sea will capture all tracer particles in the chaotic sea, since those particles eventually visit all locations in the chaotic sea. In contrast, a capture unit located so that it is always entirely within a nonchaotic island captures only a subset of tracers in the island, namely those whose trajectories intersect the unit, and none from the chaotic sea. However, a capture unit located in the chaotic sea for one portion of the flow period and in an island for the other portion eventually captures all tracers in the chaotic sea as well as some tracers from the island. It is this time-dependent character of the flow capture problem that is the focus here, namely, to consider how to optimally locate capture units based on the flow structure. Essentially, we are interested in connecting the fixed position of an arbitrary capture unit, which is Eulerian in character, with the capture of tracers advected by the flow field, which is Lagrangian in character.

As an example of flow capture, consider a capture unit with diameter $\delta = 0.1$ in the center of the domain, i.e., at (1, 0.5), in a flow with $\epsilon = 0.05$. Figure 3 shows the initial locations of tracer particles located on a 100×200 grid, indicating which are captured during the flow period intervals: 0–10, 10–10^2, 10^2–10^3, and 10^3–10^4. At this location (black circle), the unit eventually captures all particles in the chaotic sea. Figure 3 emphasizes that the time to capture tracer particles depends nontrivially on their initial positions. Approximately 34% of the total 20 000 particles are captured within the first ten periods, 24% are captured between 10 and 10^2 periods, 11% are captured between 10^2 and 10^3 periods, and only 2% are captured between 10^3 and 10^4 periods. Most of the particles captured between 10^3 and 10^4 periods are initially located

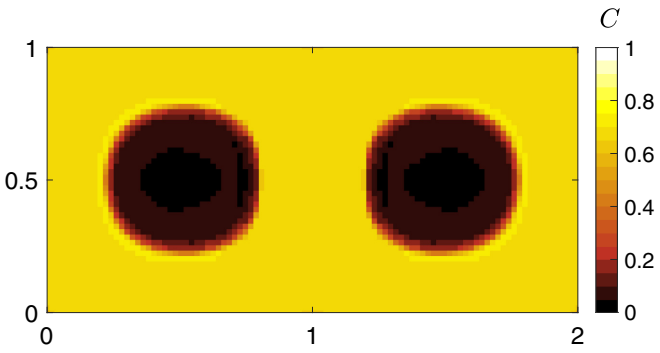

FIG. 4. Capture capability C for cells in a $M_{\text{box}} = 50\times100$ square tiling of the domain with $N_{\text{tr}} = 200\times400$ uniformly distributed initial tracer particles. $\epsilon = 0.05, t = 1000$.

around the boundaries between nonchaotic islands and the chaotic sea, regions where Cantori are likely to be present. Further note that the remaining 29% of the particles are in the nonchaotic islands and, as a result, are not captured by a capture unit at this location (white regions in Fig. 3).

Smith *et al.* [16] considered a grid of 50 possible locations for placing circular capture units with the same diameter δ and calculated the fraction of uncaptured particles after 1000 periods. To investigate the local capture capability at higher resolution, we divide the domain into a uniform grid of M_{box} boxes (squares) and calculate the fraction of N_{tr} initial tracer particles captured by each individual box, the capture capability $C(t)$, at time t, assuming that no other boxes are capturing any particles.

Continuing with the example of $\epsilon = 0.05$, we plot $C(t = 1000)$ in Fig. 4. It is evident that different regions of the flow exhibit different capture capability. C is largest (lightest) near the left (right) edge of the main left (right) gyre. C is smallest (darkest) at the gyre centers. To understand the relationship between capture capability and flow characteristics, the next sections focus on identifying transport barriers and other structures in the flow and characterizing the movement of the chaotic and nonchaotic regions over the period of the flow.

IV. CHARACTERIZING FLOW STRUCTURES

Methods for detecting barriers to transport can be categorized into two groups: (1) geometric methods that focus on concepts of invariant manifolds [38,40–45] and (2) probabilistic methods, which consider almost-invariant sets [46]. Hadjighasem *et al.* [47] provide a comprehensive review of 12 different methods including both geometric and probabilistic approaches to detect coherent structures in two-dimensional, time-aperiodic flows, comparing the strengths and weaknesses of each method.

A commonly used geometric method computes finite-time Lyapunov exponents (FTLE) and uses them to identify Lagrangian coherent structures (LCS) [22,48–59]. The alternative probabilistic approach calculates almost-invariant sets via transfer operators to identify regions that interact minimally with their surroundings [60–63]. The main difference between the two approaches is that the FTLE is applicable to detecting flow separation over short times, while the transfer operator is more practical for detecting almost-invariant sets over long times. For our work identifying structures in the double-gyre flow, which is a periodic, nonautonomous flow, we focus on detecting long-time structures since the time for significant pollutant capture to occur in geophysical flows is typically much longer than the period of the flow.

Rather than employing the transfer operator approach directly to detect flow structures, here we introduce a numerical approach connecting the Lagrangian particle motion with the Eulerian framework that combines aspects of the Poincaré map with the Lyapunov exponent approach. The goal is to differentiate nonchaotic and chaotic regions in space and time by computing the separation between two tracer points initially separated by a very small distance along the same instantaneous streamline of the velocity field. This information is then used to distinguish nonchaotic regions from the chaotic sea over the entire cycle of the flow over many periods. To do this, we utilize the concept of the Lyapunov exponent, which is a signature of chaos [29]. Specifically, given an initial point m_0 and a nearby point $m_0 + \delta_0$ on the same instantaneous streamline, where δ_0 is infinitesimally small, the separation between the two points is δ_n after n periods of the flow. If $|\delta_n| \approx |\delta_0|e^{n\lambda}$, then the Lyapunov exponent λ is defined as

$$\lambda \approx \frac{1}{n} \ln \left| \frac{\delta_n}{\delta_0} \right|, \tag{2}$$

where a positive Lyapunov exponent indicates a chaotic trajectory. In our implementation, we pick an initial point $(x(0), y(0))$, and then find a nearby point $(x'(0), y'(0))$ along the same instantaneous streamline according to

$$x'(0) = x(0) + v_x(x(0), y(0), t = 0)\tau, \tag{3a}$$

$$y'(0) = y(0) + v_y(x(0), y(0), t = 0)\tau, \tag{3b}$$

where τ is many orders of magnitude less that the flow period. Since the two points are on the same instantaneous streamline, they fall on the same side of any instantaneous barrier to transport. Then, the locations of the two tracer points $(x(0), y(0))$ and $(x'(0), y'(0))$ are determined at flow time t such that

$$(x(t), y(t)) = \Phi^t(x(0), y(0)), \tag{4}$$

$$(x'(t), y'(t)) = \Phi^t(x'(0), y'(0)), \tag{5}$$

where Φ^t is the time dependent flow map, in this case the tracer position defined by the double-gyre velocity field of Eq. (1), evaluated over time t. The separation between the two initially close points after time t is

$$\Delta(t) = \sqrt{(x(t) - x'(t))^2 + (y(t) - y'(t))^2}. \tag{6}$$

If $(x(0), y(0))$ is in a chaotic region, Δ grows with t so its value is eventually on the order of the domain size; if $(x(0), y(0))$ is in a nonchaotic region, Δ remains small. Here we choose $\tau = 10^{-15}$, so that the maximum initial distance between $(x(0), y(0))$ and $(x'(0), y'(0))$ is $\sqrt{2}\pi A\tau \approx 2\times10^{-15}$. The calculation is insensitive to the exact value of τ, e.g., $\tau = 10^{-13}$ produces nearly identical results.

To demonstrate how Δ differentiates chaotic trajectories from nonchaotic trajectories, Fig. 5 shows stroboscopic maps

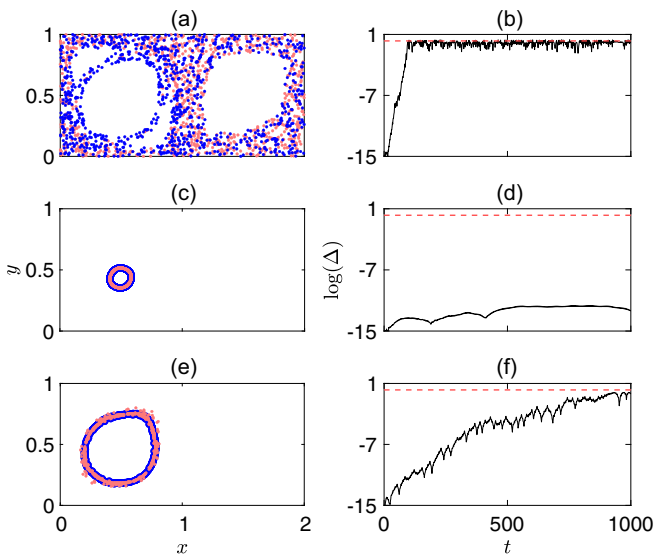

FIG. 5. Separation of two initially nearby points for three initial conditions $(x(0), y(0))$: (a), (b) in the chaotic sea $= (1, 0.5)$; (c), (d) in an island $= (0.55, 0.5)$; (e), (f) starting on a Cantorus $= (0.78, 0.5)$. (left column) pink (light gray) dots denote (x, y) and blue (dark gray) dots denote (x', y') (see text). In (c) and (e), (x', y') data are partially obscured by (x, y) data. $\epsilon = 0.05, t = 0, 1, 2, \ldots, 1000$. The dashed line in (b), (e), and (f) indicates the threshold value $\Delta = \sqrt{2}$ for determining if orbits enter the chaotic sea.

for three tracer point pairs starting at different initial positions with $\epsilon = 0.05$, where the chaotic sea and nonchaotic islands have approximately equal areas [16]. Consider, first, a tracer point at $(x(0), y(0)) = (1, 0.5)$, which is in the chaotic sea at $t = 0$ according to Fig. 2(b). Figure 5(a) plots $(x(t), y(t))$ and $(x'(t), y'(t))$ for this initial position at each iteration, marked by pink (light gray) and blue (dark gray) dots, respectively. The map exhibits the characteristics of a point in the chaotic sea, which can traverse the entire domain except inside the nonchaotic islands. The small difference between the initial locations of the two points leads to completely different trajectories. Figure 5(b) shows the corresponding Δ after each iteration, which is initially approximately 10^{-15}, but eventually grows to nearly span the entire domain. The maximum possible value for Δ is $\sqrt{5} \approx 2.236$, corresponding to the distance between opposite corners of the domain.

Figures 5(c) and 5(d) show the results for a second example with initial point (0.55, 0.5), which lies within the large island on the left in Fig. 2(b). The trajectories of the initial point and its nearby neighbor follow essentially the same trajectory. For this initial condition, Δ remains small, reaching a maximum of less than 10^{-11} after 1000 periods, as shown in Fig. 5(d), consistent with a point within a nonchaotic KAM island, since KAM tori act as absolute transport barriers [38,64–66]. In fact, the very small value of Δ in this case indicates that the initial particle and its nearby neighbor remain very close to one another over 1000 periods as they traverse an approximately circular path near the center of the nonchaotic region together.

Last, Fig. 5(e) shows an intermediate case $(x(0), y(0)) = (0.78, 0.5)$ for a tracer point that is initially on a Cantorus located on the edge of the left large nonchaotic island and chaotic sea in Fig. 2(b). The stroboscopic map for $(x(0), y(0))$ shows that the point remains in the vicinity of the Cantorus at first, but then meanders further from it as t approaches 1000. The plot of Δ for this case [Fig. 5(f)] indicates that the trajectory is chaotic in that it exhibits exponential separation for $t < 500$. At longer times, the separation is slowed due to the fractal structure of the Cantorus [36,38,67,68] which temporarily blocks the point from reaching the chaotic sea. At longer times, the tracer eventually escapes into the greater chaotic sea ($t \approx 1200$ for this example).

Based on these examples, it is evident that the value of Δ can be used as an indicator of the nature of the flow. The nonchaotic islands are constrained to be within either the left or right halves of the domain, and the chaotic interaction between the two gyres occurs around $x = 1$. As a result, for particles starting in nonchaotic islands, the maximum value for Δ cannot exceed the length of the diagonal of one square, i.e., $\sqrt{2}$. On the other hand, particles starting in the chaotic sea explore the entire domain and reach a maximum Δ larger than $\sqrt{2}$ within 1000 periods. Therefore, $\sqrt{2}$ is used as the threshold that defines which points are in the chaotic sea and which are in the nonchaotic islands. We remark that reaching this threshold can be time dependent, which is especially important when considering either very short times or the behavior of chaotic points bounded by KAM islands and Cantori.

This method to distinguish whether the trajectory of a tracer particle is chaotic or nonchaotic can be used to classify any point in the flow at a given phase as either being in the chaotic region or in a nonmixing island. Specifically, we introduce a general numerical algorithm (not specific to the double-gyre flow) for identifying those structures while simultaneously determining regions of the domain that the tracer particles visit over many periods of the flow. Algorithm 1 is based on seeding tracer particles (points) throughout the domain and determining the maximum separation $\Delta^{\max}$ for each tracer trajectory.

Algorithm 1: Determining chaotic trajectories and $\overline{F}$

Data: $\omega, \epsilon, A, t_{\max}, \Delta t << 1, M_{\text{box}}$
Result: average chaotic fraction $\overline{F}$
Initialize $(x_i(0), y_i(0))$ for N_{tr} tracer particles
Divide the domain into M_{box} equal boxes;
for $i = 1 : N_{\text{tr}}$ **do**
  Find nearby point $(x_i'(0), y_i'(0))$ by Eq. (3);
  Calculate the trajectory of $(x_i(t), y_i(t))$ and $(x_i'(t), y_i'(t))$ for each Δt for $0 \leqslant t \leqslant t_{\max}$ by Eqs. (4) (5);
  Use Eq. (6) to determine $\Delta_i^{\max}$;
  if $\Delta_i^{\max} > \sqrt{2}$ **then**
    $traj_i =$ chaotic;
  else
    $traj_i =$ nonchaotic;
for *each* Δt **do**
  Determine the fraction F_j of particles with chaotic trajectories in each box j;
return $\overline{F}_j$ by averaging F_j at all timesteps

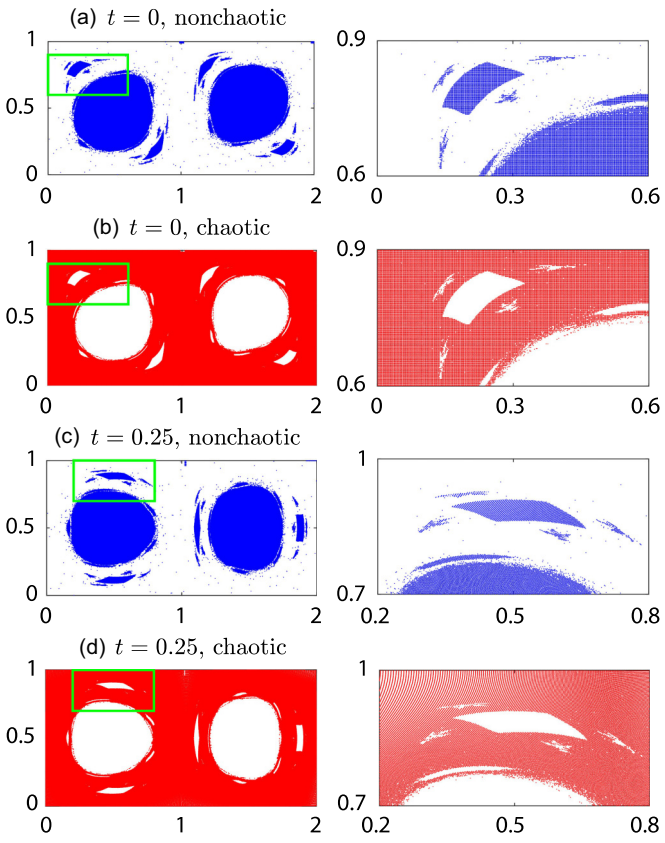

FIG. 6. Tracer particle locations at (a) $t = 0$ for particles with nonchaotic ($\Delta^{\max} < \sqrt{2}$) trajectories; (b) $t = 0$ for particles with chaotic ($\Delta^{\max} > \sqrt{2}$) trajectories; (c) $t = 0.25$ for particles with nonchaotic ($\Delta^{\max} < \sqrt{2}$) trajectories; and (d) $t = 0.25$ for particles with chaotic ($\Delta^{\max} > \sqrt{2}$) trajectories. Rectangle indicates expanded region in right column. Tracers are initially positioned on a uniform $N_{\text{tr}} = 500\times1000$ grid. $\epsilon = 0.05$, $t = 1000$.

Figure 6 shows the sets of initial particle locations for which $\Delta^{\max} < \sqrt{2}$ (particles with nonchaotic trajectories) or $\Delta^{\max} > \sqrt{2}$ (particles with chaotic trajectories). The result of this step (the first loop in Algorithm 1) indicates whether a particle starts in one of the nonchaotic islands [blue (dark gray)] or the chaotic sea [red (light gray)] at $t = 0$ in Figs. 6(a) and 6(b). The slight differences between the two sets, which are complements to one another, result from the finite size of the data symbols used in the plot. To clarify the details of small islands, the second column of Fig. 6 shows magnified views of the boxed regions in the first column. Figures 6(c) and 6(d) show the location of nonchaotic or chaotic particles at a different time $t = 0.25$, which illustrates the movement of the islands and changes in the boundary between the nonchaotic islands and the chaotic sea.

The field $\overline{F}$ indicates the average fraction of chaotic tracer particles at locations (boxes) across the entire flow domain. There are three different regions that can be identified in the flow, shown in Fig. 7:

(1) *Nonchaotic region:* $\overline{F} = 0$, all trajectories that transit this region are nonchaotic.

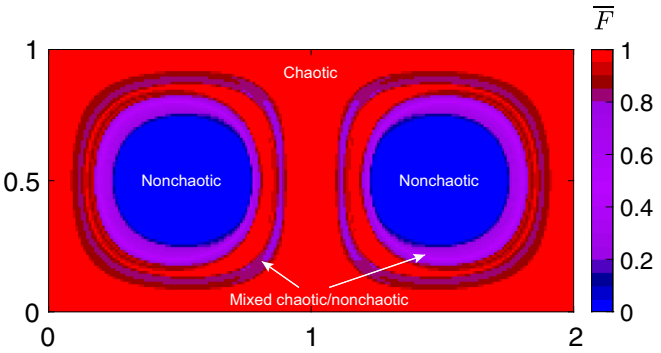

FIG. 7. Average chaotic fraction $\overline{F}$ on a $M_{\text{box}} = 100\times200$ square tiling with time step $\Delta t = 0.005$. $\epsilon = 0.05$, $t_{\max} = 1000$.

(2) *Chaotic region:* $\overline{F} = 1$, all trajectories that transit this region are chaotic.

(3) *Mixed chaotic-nonchaotic regions:* $0 < \overline{F} < 1$, both chaotic and nonchaotic trajectories transit this region.

The value of $\overline{F}$ throughout the flow domain in Fig. 7 displays the regions evident in Fig. 2(c), a ringlike structure surrounding each large nonchaotic region, except that $\overline{F}$ represents an Eulerian viewpoint based on the types of particles passing a particular location in the flow. The red (light gray) region is always chaotic, and the blue (dark gray) region is always nonchaotic. Particles passing through mixed regions of the flow may be either nonchaotic or chaotic, depending on the phase in the period of the flow. The coloring represents the fraction of particles passing that point in the flow that are chaotic.

Note that the number of initial particles N_{tr} and the number of boxes M_{box} covering the flow domain can be varied as needed to account for computational constraints and resolution requirements. The slight blurring of the structures in Fig. 7 is due to the finite grid resolution with which it was generated (100×200); sharper structural details can be revealed by using finer grid resolution. Furthermore, the value of $1/\Delta t$ is equivalent to the increment in the phase θ, and it is necessary to choose Δt small enough to resolve the continuously varying locations of the mixed chaotic-nonchaotic regions associated with the positions of the small islands evident in Fig. 2(c).

V. FLOW CONDITIONS AND CAPTURE CAPABILITY

The flow regions shown in Fig. 7 can explain most features of the capture capability C visible in Fig. 4. The highest C value regions in Fig. 4 (lightest) occur near the periphery of the gyres (not in the fully chaotic region) and correspond to the mixed chaotic-nonchaotic regions surrounding the nonchaotic cores in Fig. 7 for which a capture unit can remove all pollutant particles from the chaotic sea as well as a significant amount of particles from the central nonchaotic islands. There is also a slight increase in C corresponding to the outer rings labeled "mixed" in Fig. 7 due to the additional particles captured there from the two small satellite islands, although it is not evident in Fig. 4 as the fraction of particles in the two small islands is quite small. Just inward from the highest capture regions in Fig. 4, C decreases rapidly [orange (dark

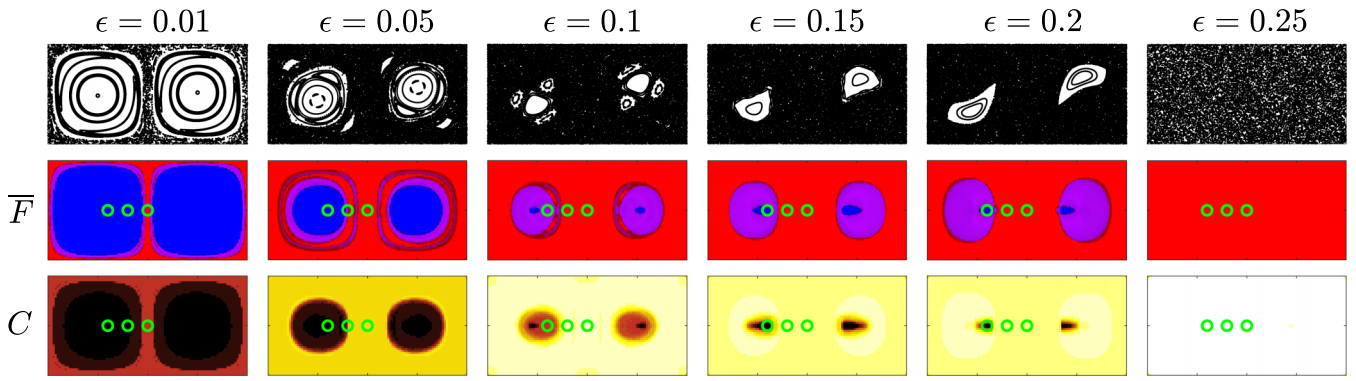

FIG. 8. Flow and capture characteristics (rows) for $\epsilon = 0.01, 0.05, 0.1, 0.15, 0.2, 0.25$ (columns). Row 1: Poincaré maps at $\theta = 0$. Row 2: Average chaotic fraction, $\overline{F}$. Row 3: Capture capability, $C(t = 1000)$. Color bars for rows 2 and 3 correspond to those in Figs. 7 and 4, respectively. Maximum C within each unit and $C_{\text{unit}}(t = 1000)$ are given in Table I.

gray) and black regions], which corresponds to the always nonchaotic regions in Fig. 7. A capture unit in the mixed chaotic-nonchaotic region (lightest) will most effectively capture particles, while a capture unit in the fully nonchaotic region (darkest) will be the least effective.

The value of C, which is evaluated over a fine grid, can also be related to the capture capability of a capture unit that spans a finite area such as the circular capture unit in Fig. 3. However, it is important to note that length scales become important here. Returning to our original motivation for this research, that of carbon capture from the atmosphere, the flow domain of interest would likely be a large region and the length scale of structures in the flow would likely be much larger than the scale of any reasonably sized capture unit. In this case, analysis based on a fine grid like that in Fig. 4 would be appropriate, since the capture unit would represent a mere single point in the flow domain (or a box in our analysis). On the other hand, it is also reasonable to think in terms of an array or line of capture units (analogous to a wind turbine farm for power generation). In this case the length scale of the array of capture units could be on the scale of structures in the flow field. Thus, we consider finite area capture units like that in Fig. 3. Not only does this allow us to account for a local group of capture units, it also allows us to consider more deeply the underlying relation between the flow field and the capture capability to elucidate some of the underlying issues related to capture unit placement and effectiveness.

We specifically consider circular capture units to avoid issues related to the orientation of the capture unit. For instance, if we considered a linear array of capture units, the orientation of the array with respect to the predominant flow direction would be critical with respect to the capture capability, an aspect we consider in a later section. Using a circular capture unit avoids this issue. Nevertheless, for the circular capture unit with diameter $\delta = 0.1$ in Fig. 3, its periphery can be approximated by a set of adjacent grids boxes used to compute C. A lower bound on the capture capability for the circular unit is the maximum C for any of the grids boxes within its periphery since the particles captured by any small box must also enter the large circular unit. In Fig. 3 the maximum C for all grids boxes within the circular capture unit at $(1, 0.5)$ is 69%, and the capture capability for the circular unit itself is 69%.

With this background we now consider how the nature of the flow affects the chaotic fraction $\overline{F}$ and capture capability C. The flow structure is varied by considering different values of the flow parameter, $\epsilon = 0.01, 0.05, 0.1, 0.15, 0.2, 0.25$, as shown in the columns of Fig. 8. Rows in Fig. 8 display the following: the first row shows the Poincaré maps; the second row shows $\overline{F}$; the third row plots C.

Consider the second column in Fig. 8 for $\epsilon = 0.05$, which corresponds to the conditions in Figs. 2(b) and 2(c), 4, and 7, in which there are two large nonmixing islands plus four smaller islands, two of which circulate around each of the larger islands (first row). As a result, there are two large regions where all trajectories are nonchaotic surrounded by a chaotic-nonchaotic ring (second row). The capture capability is optimal at the edge of the large nonchaotic cells, and the remainder of the domain is chaotic with a slightly lower capture capability (third row).

Superimposed on the second and third rows are three circular capture units ($\delta = 0.1$) at $(0.6, 0.5)$, $(0.8, 0.5)$ and $(1, 0.5)$. By comparing the value of $\overline{F}$ and the ultimate capture capability C at these different locations, the interaction of a capture unit with the flow structures can be visualized and explained. For $\epsilon = 0.05$, a single capture unit centered at $(0.6, 0.5)$, which is entirely within the left nonchaotic region, captures only a portion of the nonchaotic particles initially located in the island. On the other hand, a capture unit at $(0.8, 0.5)$, which intersects all three region types (nonchaotic, chaotic-nonchaotic, and chaotic), captures a part of the nonchaotic particles initially in the island as well as all chaotic particles. The capture unit at $(1, 0.5)$, which is entirely in the chaotic region, captures only chaotic particles. Because the unit at $(0.8, 0.5)$ should capture all of the chaotic particles and some nonchaotic particles from the left gyre ultimately, the maximum value of C within the unit is larger than units $(0.6, 0.5)$ and $(1, 0.5)$, where unit $(0.6, 0.5)$ captures the least. In fact, the maximum C for any of the grid boxes within the capture unit circle is 5% for the $(0.6, 0.5)$ unit, 68% for the $(0.8, 0.5)$, and 69% for the $(1, 0.5)$ unit, compared to values for the entire unit, denoted as $C_{\text{unit}}(t = 1000)$, of 6%, 75%, and 69%, respectively (see Table I).

Consider now the capture process for other values of ϵ. For $\epsilon = 0.01$ (first column in Fig. 8), most of the domain is nonchaotic as evident from the Poincaré map in the first

TABLE I. Maximum C within each unit, C_{unit} at $t = 1000$, and corresponding line styles in Figs. 10 and 11.

Unit	ϵ	Max C	C_{unit}	Line style	Fig.
(0.6,0.5)	0.01	2%	4%		10(a)
	0.05	5%	6%		10(a)
	0.1	25%	27%		10(c), 11(c)
	0.15	7%	15%		10(c), 11(c)
	0.2	40%	76%		10(c), 11(c)
	0.25	100%	100%		10(b), 11(b)
(0.8,0.5)	0.01	4%	13%		10(a)
	0.05	68%	75%		10(c), 11(c)
	0.1	91%	91%		10(b), 11(b)
	0.15	89%	89%		10(b), 11(b)
	0.2	90%	90%		10(b), 11(b)
	0.25	100%	100%		10(b), 11(b)
(1,0.5)	0.01	23%	28%		10(c), 11(a)
	0.05	69%	69%		10(b), 11(a,b)
	0.1	91%	91%		10(b), 11(a,b)
	0.15	89%	89%		10(b), 11(a,b)
	0.2	90%	90%		10(b), 11(a,b)
	0.25	100%	100%		10(b), 11(a,b)

row, with two large islands. The resulting average chaotic fraction $\overline{F}$ in the second row is small over much of the domain as a result. The capture capability C is low even in the chaotic region and small mixed chaotic-nonchaotic region surrounding the nonchaotic regions (third row) because most tracer particles remain in the large nonchaotic islands and few are in the chaotic sea. Two capture unit locations, $(0.6, 0.5)$ and $(0.8, 0.5)$, are fully within the nonchaotic region and can capture only nonchaotic particles. The unit at $(1, 0.5)$ is primarily in the chaotic region, but it also covers a bit of the mixed chaotic-nonchaotic region, so it captures chaotic particles as well as a small part of nonchaotic particles. But because the chaotic region is relatively small for $\epsilon = 0.01$, the unit captures far fewer particles overall than occurs for other values of ϵ corresponding to larger chaotic regions in the first row (see Table I).

When $\epsilon = 0.1$ (third column in Fig. 8), three small islands surround each of the large islands, but the large islands are smaller compared to those at smaller ϵ, thereby increasing the region with a high chaotic fraction (second row) and resulting in a high capture capability (third row) throughout much of the domain. The $(0.6, 0.5)$ unit is entirely within the mixed chaotic-nonchaotic region of the left gyre, so it captures nonchaotic particles in the left gyre as well as all chaotic particles. However, the value of C is not the highest of the three units since it takes longer than 1000 periods for the $(0.6, 0.5)$ unit to capture all chaotic particles. Units at $(0.8, 0.5)$ and $(1, 0.5)$ are both located in the chaotic region, and capture similar quantities of chaotic particles (see Table I).

When $\epsilon = 0.15$, the small islands disappear, the two large islands become larger than for $\epsilon = 0.1$, and the total area of chaotic sea decreases slightly. This is reflected in the value of C being slightly lower in the chaotic region than for $\epsilon = 0.1$. The $(0.6, 0.5)$ unit overlaps both the nonchaotic region and the mixed chaotic-nonchaotic region, but captures far fewer points than the units in the chaotic region over 1000 periods of the flow (see Table I). For much of the area corresponding to the mixed chaotic-nonchaotic region in the second row, it is evident in the third row that the value of C is higher than that in the chaotic region.

For $\epsilon = 0.2$, there are still two nonchaotic islands but their shapes result in the mixed chaotic-nonchaotic region increasing in size so that the region with high C also increases in size. Unlike the $\epsilon = 0.15$ case, the $(0.6, 0.5)$ unit captures a significant fraction of particles even though it overlaps nonchaotic and mixed chaotic-nonchaotic regions (see Table I). The other two capture unit locations still capture more chaotic particles, similar to the $\epsilon = 0.15$ case.

Finally, when $\epsilon = 0.25$, the entire region is chaotic, so the capture capability C over the entire domain can reach 1, and the capture capability for all three units is the same.

Considering the entirety of Fig. 8, the overall capture capability depends primarily on the location of the capture unit relative to the chaotic and nonchaotic regions of the flow. However, the capture capability also depends on the nature of the underlying flow, noting that C varies substantially with ϵ for the capture unit at $(1, 0.5)$.

VI. TIME DEPENDENCE OF CAPTURE

The number of particles captured by a unit also depends on time. To consider this, we plot the initial positions of particles captured between 0–10^1, 10^1–10^2, 10^2–10^3, and 10^3–10^4 flow periods by capture units at the three different locations in the first three rows of Fig. 9 (similar to Fig. 3). The differences are striking. Capture units at $(0.6, 0.5)$ in the first row are far less efficient, requiring 10^2 to 10^4 periods to capture particles in the chaotic region, than capture units at $(0.8, 0.5)$ and $(1, 0.5)$ in the second and third rows, which require less than 10^2 periods. Likewise, flow conditions associated with large nonchaotic regions at low values of ϵ are ineffective because few particles can be extracted from the flow (large white areas).

To further consider the time dependence of capture, it is helpful to categorize the capture in terms of the average chaotic fraction, $\overline{F}$ (row 2 of Fig. 8). Recall that a capture unit can be placed in the nonchaotic region, where only particles with nonchaotic trajectories can be captured, the mixed chaotic-nonchaotic region, where particles with nonchaotic and chaotic trajectories can be captured, or the chaotic region, where only particles with chaotic trajectories can be captured. To quantify the effectiveness of capture units in different locations we consider the fraction of particles in the domain captured by a capture unit as a function of time, $C_{\text{unit}}(t)$, and organize the results into three groups in Fig. 10 according to the average value of $\overline{F}$ within the capture unit, denoted as $\overline{F}_{\text{unit}}$: (a) nonchaotic regions ($\overline{F}_{\text{unit}} < 1\%$), (b) chaotic regions ($\overline{F}_{\text{unit}} > 99\%$), and (c) mixed chaotic-nonchaotic regions ($1\% < \overline{F}_{\text{unit}} < 99\%$). Note that the chaotic sea may contain a number of very small islands [31], so $\overline{F}_{\text{unit}} < 1$. The three groups of outlined boxes in the first three rows of Fig. 9 correspond to the three conditions categorized in Fig. 10. With this categorization, the interaction of a capture unit with the flow structures at different timescales visualized in Fig. 9 can be be connected to the differences in the time dependence of capture fractions for different units in Fig. 10.

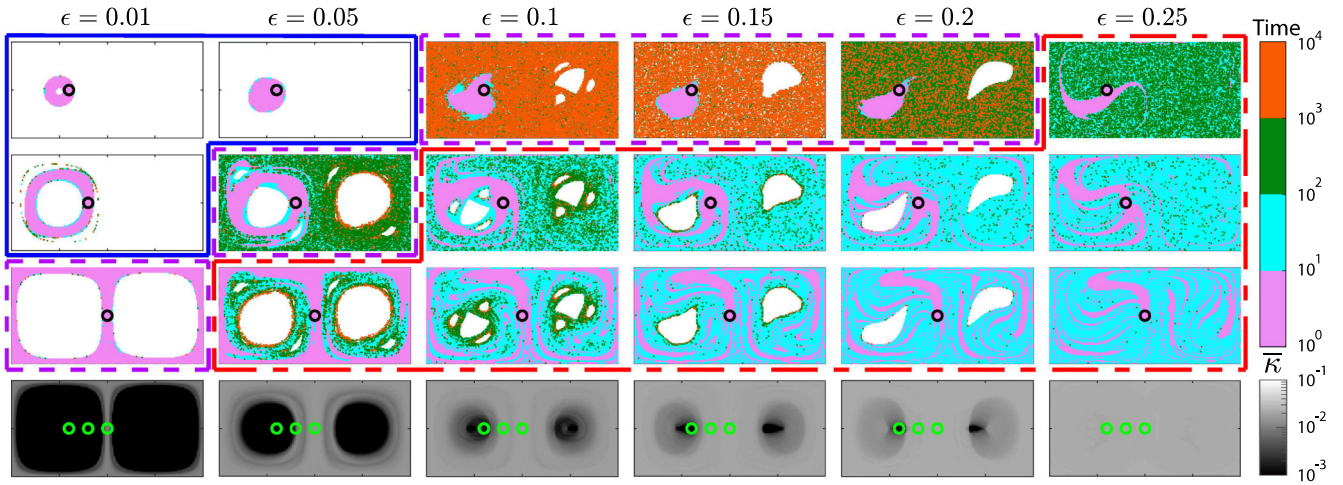

FIG. 9. Capture times for initial positions of tracer particles (on a 100×200 grid) by unit at (0.6, 0.5) (row 1), (0.8, 0.5) (row 2) and (1, 0.5) (row 3). Box outlines in rows 1–3 indicate capture units in: nonchaotic regions (solid blue), mixed chaotic-nonchaotic regions (dashed magenta), and chaotic regions (long-short dashed red), corresponding to the three categories in Fig. 10. Row 4: Average separation rate $\overline{\kappa}$ determined by dividing the domain into 100×200 boxes and calculating the separation rate for trajectories of tracer particles with initial positions on a 100×200 grid through each box location for ten periods using a time step $\Delta t = 0.005$.

For units entirely in nonchaotic regions [Fig. 10(a)], the capture fraction $C_{\text{unit}}(t)$ increases nearly linearly in the first few periods (see below) and then saturates. The three cases can capture only nonchaotic particles, and they do so quickly within the first ten periods (Fig. 9). For $\epsilon = 0.01$, the (0.8, 0.5) unit captures particles more rapidly than the (0.6, 0.5) unit as it is further from the center of the gyre and captures the particles in a larger diameter annular region, as shown in Fig. 9. Although the (0.6, 0.5) unit is fully within the nonchaotic region for both $\epsilon = 0.01$ and $\epsilon = 0.05$, slightly more particles are captured at $\epsilon = 0.05$ because the slight side-to-side movement of the large gyre brings more particles to the capture unit.

For units entirely in the chaotic region [Fig. 10(b)], nearly all conditions reach a plateau within about 100 periods after capturing the majority of particles in the chaotic sea. This is also evident in the boxes outlined in long-short dashes (red online) in Fig. 9, where in nearly all cases particles throughout the chaotic region are captured in 100 periods or fewer. At $\epsilon = 0.25$, the plateau of $C_{\text{unit}}(t)$ in Fig. 10(b) reaches 1 since the entire domain is chaotic. An interesting result is that although the unit at (0.6, 0.5) with $\epsilon = 0.25$ is in the chaotic sea, it is much slower in capturing particles than all the other cases where the capture unit is in the chaotic sea [evident in Fig. 10(b) and the upper right of Fig. 9]. It seems that even though no large nonchaotic regions are present, this location, which is in a location corresponding to that of nonchaotic regions at lower values of ϵ, is much slower in capturing particles than locations farther from nonchaotic regions at lower ϵ. The cases with $\epsilon = 0.1$, 0.15 and 0.2 have a similar plateau around 0.9 in Fig. 10(b) even with different shapes of nonchaotic islands evident in the Poincaré maps in Fig. 8. However, for $\epsilon = 0.1$, the plateau is slightly higher because of the larger area of the chaotic sea. For different units with the same ϵ, the (0.8, 0.5) unit captures particles more slowly than the (1, 0.5) unit, but still reaches the same asymptotic value,

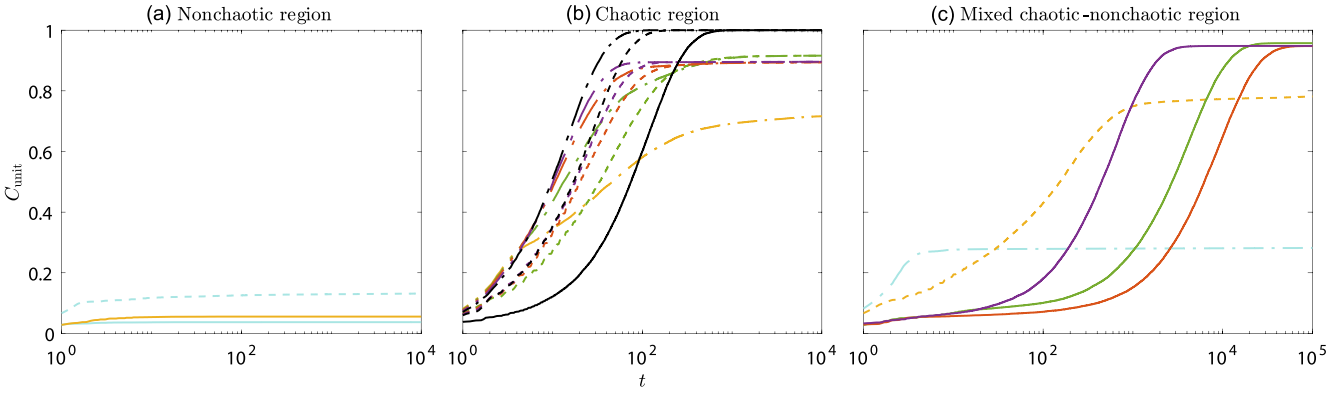

FIG. 10. Capture fraction for a circular unit, $C_{\text{unit}}(t)$, at different ϵ and unit locations. (a) Units in nonchaotic regions ($\overline{F}_{\text{unit}} < 1\%$). (b) Units in chaotic region ($\overline{F}_{\text{unit}} > 99\%$). (c) Units in mixed chaotic-nonchaotic regions ($1\% < \overline{F}_{\text{unit}} < 99\%$). Line colors (gray scale intensities) correspond to different values of ϵ, and line styles correspond to different unit locations as given in Table I.

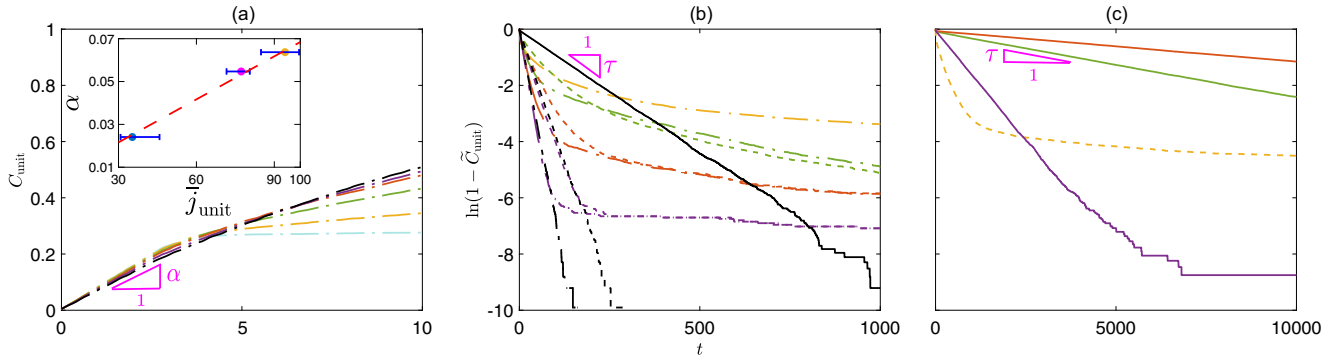

FIG. 11. (a) Capture fraction $C_{\text{unit}}(t)$ for circular unit at $(1, 0.5)$ with different ϵ at short times. Inset: Slope α (fitted over the first five periods) averaged over six ϵ values for three units at $(0.6, 0.5)$, $(0.8, 0.5)$ and $(1, 0.5)$, from lower left to upper right, vs time-averaged flux $\bar{j}_{\text{unit}}$ into each unit. Error bars indicate minimum and maximum values for six distinct ϵ. Normalized capture fraction $\ln[1-\tilde{C}_{\text{unit}}(t)]$ vs time t for units in (b) chaotic region and (c) mixed chaotic-nonchaotic regions. Here $\tilde{C}_{\text{unit}}(t) = C_{\text{unit}}(t)/C_{\max}$, where $C_{\max} = C_{\text{unit}}(t = 10^4)$ for chaotic region and $C_{\max} = C_{\text{unit}}(t = 10^5)$ for mixed chaotic-nonchaotic regions. Line colors (gray scale intensities) correspond to different ϵ, and line styles correspond to different unit locations as indicated in Table I.

as shown in Fig. 10(b). This occurs because the flux passing the perimeter of the unit is higher for the $(1, 0.5)$ unit than for the $(0.8, 0.5)$ unit due to its location in the flow, as will be shown shortly. A noticeable exception in Fig. 10(b) is the case with $\epsilon = 0.05$ and unit $(1, 0.5)$, where the value of $C_{\text{unit}}(t)$ is much smaller than for the other condition after 100 periods and still slowly increasing (note particles captured between 10^3 and 10^4 periods in Fig. 9). The lower value is simply due to the smaller chaotic region for $\epsilon = 0.05$ (evident in Fig. 9). More interestingly, the slow increase in $C_{\text{unit}}(t)$ is due to the Cantori regions that surround both large nonchaotic islands, resulting in a slow leakage of particles around the edge of the nonchaotic islands into the chaotic sea.

For units in the mixed chaotic-nonchaotic regions shown in Fig. 10(c), there is an initial capture interval (about ten periods) in which particles from the nonchaotic regions are captured, followed by slow capture of all the particles from the chaotic sea (see boxes outlined in dashed magenta in Fig. 9). Note that the case with $\epsilon = 0.01$ and the unit at $(1, 0.5)$ is an exception, as it is mostly located in the chaotic region, and captures all chaotic particles in a short time as well as some nonchaotic particles. However, the overall capture capability for this unit is small because the area of the chaotic sea is small (Fig. 9). For all units in mixed chaotic-nonchaotic regions, capture of particles from the chaotic sea is ten to 100 times slower than for capture units always in chaotic regions [comparing Fig. 10(c) to Fig. 10(b)] due to the intermittent exposure of the unit to the chaotic flow (i.e., $\overline{F} < 1$). Units with the same ϵ in the mixed chaotic-nonchaotic region eventually capture more particles than units in the chaotic region, but take longer to do so. For example, the $(0.6, 0.5)$ unit captures more particles than the $(0.8, 0.5)$ and $(1, 0.5)$ units when $\epsilon = 0.1, 0.15$ or 0.2, evident as higher plateaus in Fig. 10(c) than in Fig. 10(b).

The temporal aspects of the capture process are characterized by three timescales. In the first, which occurs at short times, advection dominates and $C_{\text{unit}}(t)$ initially grows linearly as illustrated in Fig. 11(a) for a unit at $(1, 0.5)$ for all six values of ϵ. For the first five periods, the curves are nearly identical with similar slope α, while for longer times, the $\epsilon = 0.01$ curve is nearly flat and the curves for other values of ϵ increase slower than initially, consistent with a second timescale in the flow. The duration of the linear capture regime is simply the time for a particle trajectory to complete an approximate orbit at the location of the capture unit. At the limit $\epsilon = 0$, all tracer particles that can be captured are captured in the first orbit. Similarly, we can determine α for units at $(0.6, 0.5)$ and $(0.8, 0.5)$. The slope of $C_{\text{unit}}(t)$ for small t, α can be related to the time-averaged positive flux of the flow passing the perimeter of the unit, denoted as $\bar{j}_{\text{unit}} = \frac{1}{N_\theta}\sum_{j=1}^{N_\theta}\sum_{i=1}^{N}(\vec{v}\cdot\vec{n})_{i,j}$, where $\vec{v}$ is the velocity at the perimeter of the unit, N_θ indicates the number of different phases within one period, and N indicates different locations along the perimeter. Here we use 200 phases with a time step $\Delta t = 0.005$ and 200 uniform locations along the unit perimeter. The normal vector $\vec{n}$ points toward the center of the unit, and we consider only regions with $\vec{v}\cdot\vec{n} > 0$, i.e., inflows. The inset in Fig. 11(a) shows the relationship between α and $\bar{j}_{\text{unit}}$ for the three capture unit locations. The data for $\bar{j}_{\text{unit}}$ are the average over six values of ϵ, and the error bar indicates the maximum and minimum value of the six cases. It is clear that α depends linearly on $\bar{j}_{\text{unit}}$, and that the flux into a unit largely determines the capture rate during the first few periods.

The second timescale characterizes particles captured from the chaotic sea and is reflected in the slower increase in $C_{\text{unit}}(t)$ evident in Fig. 11(a) after the first few periods. Due to the ergodic nature of chaotic mixing [46,69–72], $C_{\text{unit}}(t)$ should be exponential in time, i.e., $C_{\text{unit}}(t) = C_{\max}(1 - e^{-t/\tau})$ or $\ln[1 - \tilde{C}_{\text{unit}}(t)] = -t/\tau$, where τ is the second timescale, which depends on the flow conditions, and $\tilde{C}_{\text{unit}}(t) = C_{\text{unit}}(t)/C_{\max}$. Figure 11(b) plots $\ln[1 - \tilde{C}_{\text{unit}}(t)]$ vs t, which shows a linear regime for all the curves. For $\epsilon = 0.25$, the linear regime extends to the plateau where $C_{\text{unit}}(t)$ asymptotes in Fig. 10(b). However, for smaller ϵ where there are still nonchaotic regions, the curves flatten at about 200 periods as most of the particles in the chaotic region are captured after which there is a slow accumulation of additional particles, evident by a deviation from a linear relation, that is associated with slow leakage from the Cantori regions. Therefore to determine τ,

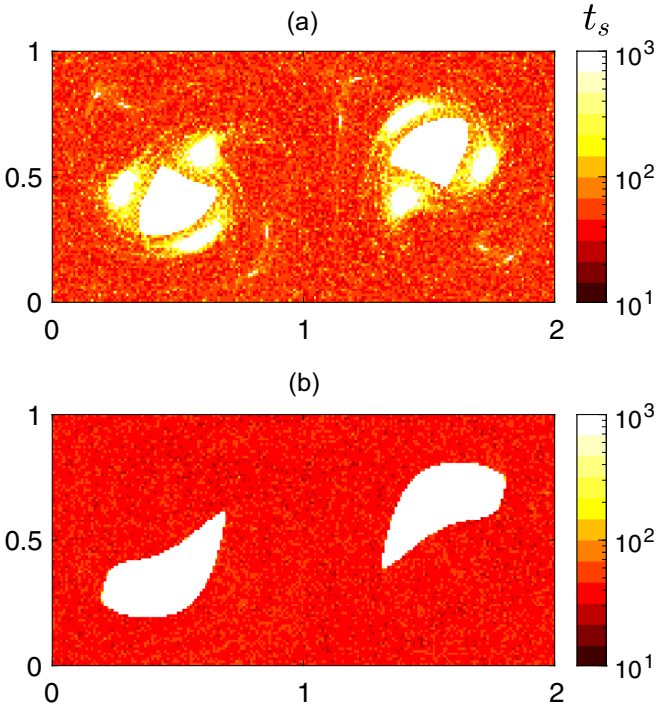

FIG. 12. Separation time t_s when particle pair separation Δ first exceeds $\sqrt{2}$ for tracer particles with initial positions on a 100×200 grid. (a) $\epsilon = 0.1$ (b) $\epsilon = 0.2$. White indicates particles for which $\Delta < \sqrt{2}$ after 1000 flow periods.

we fit the linear portion of $\ln[1 - \tilde{C}_{\text{unit}}(t)]$ vs time, which occurs after the initial advection dominated regime, and before the later and slower regime associated with capture of particles escaping from the Cantori regions.

For units in the mixed chaotic-nonchaotic region, the normalized capture fraction $\ln[1 - \tilde{C}_{\text{unit}}(t)$ vs t is shown in Fig. 11(c). Clearly, the slope τ is much lower than that for units in the chaotic region. Here we exclude the case with $\epsilon = 0.01$ at unit $(1, 0.5)$, as it is included in Fig. 11(a) and its chaotic region is relatively small compared to the area of the unit (second row of Fig. 8). Therefore it captures chaotic particles quickly but in the advection dominated regime.

At this point, it is useful to explore the factors that influence the chaotic capture rate and the slope τ. Recall that the value of $\overline{F}_{\text{unit}}$ determines the ultimate capture capability. Consider two cases in Fig. 11(c) at unit $(0.6, 0.5)$ with $\epsilon = 0.1$ and 0.2. In row 2 of Fig. 8, the value of $\overline{F}$ for this unit is greater at $\epsilon = 0.1$ than at $\epsilon = 0.2$, which is centered over a small, mostly nonchaotic region. However, Fig. 11(c) shows that τ is larger for the $\epsilon = 0.2$ case, indicating that it captures chaotic particles more quickly than for $\epsilon = 0.1$.

One explanation for this discrepancy could be that particle trajectories become chaotic faster [using our separation-based definition, Eq. (6)] for some values of ϵ than for others, keeping in mind that $\overline{F}$ is based on 1000 periods, a relatively long time given the timescales evident in Figs. 9 and 10 for some cases. To determine when particle trajectories become chaotic, we calculate the time t_s when the separation Δ first exceeds $\sqrt{2}$ for each initial particle location using a uniform seeding of particles. The result is shown in Fig. 12 for $\epsilon = 0.1$

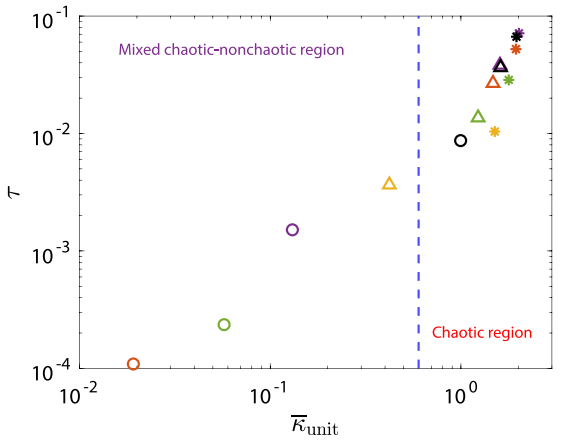

FIG. 13. Characteristic capture time τ vs average separation rate $\overline{\kappa}_{\text{unit}}$ for units in mixed chaotic-nonchaotic regions and chaotic region corresponding to Figs. 11(b), 11(c). Circle, triangle, and star symbols represent units at $(0.6, 0.5)$, $(0.8, 0.5)$, $(1, 0.5)$, respectively. Colors (gray scale intensities) for different ϵ are the same as Fig. 11.

and $\epsilon = 0.2$. Particles that separate quickly are darker, while particles for which Δ remains less than $\sqrt{2}$ for 1000 periods are white. It is evident that the chaotic particles around the islands for $\epsilon = 0.1$ take much longer to separate than any of the chaotic particles for $\epsilon = 0.2$. Even away from the islands t_s is slightly longer for $\epsilon = 0.1$ than for $\epsilon = 0.2$. Thus, even though the value of $\overline{F}$, which is calculated at 1000 periods, is high at a particular location, it is still possible that the chaotic capture rate is lower than at other locations with similar values of $\overline{F}$.

Extending this idea, we define the separation rate, $\kappa = 1/t_s$. To characterize the typical separation rate for tracer particles at locations across the domain, we divide the domain into a grid of boxes and determine the average separation rate $\overline{\kappa}$ for trajectories passing through each box over several periods (ten in this case). We consider only a short time to minimize the influence of initially distant chaotic particles with short separation times. This is similar to the method for calculating $\overline{F}$, except that instead of determining the fraction of chaotic trajectories passing through the box, we calculate the average separation rate of trajectories passing through the box, noting that nonchaotic trajectories after 1000 periods are assigned the separation rate of $\kappa = 0.001$, which overestimates the local κ values. Local κ values for various ϵ are shown in row 4 of Fig. 9. When $\overline{\kappa}$ is small, particles passing the corresponding region take longer to become chaotic.

The capture rate of a unit is also related to the flux of particles into the capture unit, which is related to the velocity field. To determine the separation rate for a circular unit, we consider the combined effect of average separation rate and flux, $\overline{\kappa(\vec{v} \cdot \vec{n})}$, for boxes along the perimeter of the unit, where we again consider only positive fluxes (into the unit). To account for the variation of velocity field over one period, we calculate the time-average separation rate for a unit as $\overline{\kappa}_{\text{unit}} = \frac{1}{N_\theta} \sum_{j=1}^{N_\theta} \sum_{i=1}^{N} \overline{\kappa}_i (\vec{v} \cdot \vec{n})_{i,j}$, similar to the way $\overline{j}_{\text{unit}}$ is calculated. The relationship between the chaotic capture slope τ and the average separation rate $\overline{\kappa}_{\text{unit}}$ is revealed in Fig. 13. For units in the mixed chaotic-nonchaotic region, the relationship between τ and $\overline{\kappa}_{\text{unit}}$ is monotonic and increasing,

which confirms that the chaotic capture rate is related to both the separation time of particles entering the unit and the flux of those particles into the unit. For units in the chaotic region, the relationship is also monotonic for the same unit with different values of ϵ.

The third timescale characterizing particle capture is evident for cases in Figs. 10(b) and 10(c) that do not reach a horizontal plateau at large times after the exponential increase of capture fraction C_{unit}. In this regime, there is a slow increase in C_{unit} as particles slowly cross the fractal mixing barriers of the Cantori bounded regions. Although characterizing this timescale is beyond the scope of this paper, we note that the relative area of Cantori regions or regions bounded by Cantori and nonmixing regions is small. Consequently, there is relatively little change in the capture fraction even after the relatively long times associated with escape from Cantori regions (as well as into Cantori bounded regions for capture units located within them).

VII. CONCLUSIONS

Given the significance of removing pollutants such as CO_2 from the atmosphere or debris from the ocean, the motivation of this research is to explore how the chaotic nature of geophysical flows can affect the removal of pollutants. This study of the double-gyre flow provides context for how to predict the effectiveness of a capture unit at an arbitrary location in a real geophysical flow, extending the work of Smith *et al.* [16] on the flow capture problem by linking the spatial variation of capture efficiency to mean locations of chaotic and nonchaotic regions in the flow. The novelty of this study is in introducing a numerical approach to characterize transport in the dynamical system and connecting it with the effectiveness of a capture unit. While a Poincaré map is useful for demonstrating the dynamical properties of a flow, it reveals flow characteristics only at a single phase. In considering the efficacy of a capture unit at a specific location in a flow, it is necessary to consider the local flow conditions at different phases during the flow cycle. By tracing chaotic and nonchaotic trajectories and calculating the average fraction of chaotic particles $\overline{F}$ throughout the domain for all phases, we identify three different regions in the flow: nonchaotic, chaotic, and mixed chaotic-nonchaotic. Therefore the study of the efficiency of an Eulerian capture unit depends on the characteristics of the behavior of passive scalars in the Lagrangian frame.

Based on the relation of the capture capability to the local flow structures averaged over a flow period, it is evident that a capture unit in a mixed chaotic-nonchaotic region is most effective, as it can capture all of the chaotic particles and some of the nonchaotic particles. However, since it is not always in the chaotic region, it takes longer to capture the chaotic particles than a unit always in the chaotic region. Thus, the capture timescale is another factor that influences the overall capture capability, especially for capture units in mixed chaotic-nonchaotic regions.

For units in mixed chaotic-nonchaotic or chaotic regions, the capture occurring while the unit is exposed to chaotic flow is the most critical for determining the capture rate and efficiency of a unit. However, the separation time for chaotic particles and the flux through the perimeter of a capture unit are also both influential factors.

Of course, actual geophysical flows differ from the double-gyre flow model used here [Eq. (1)] in that they are not time periodic and they are three-dimensional, both of which can weaken or destroy the invariant surfaces bounding the KAM islands. That said, geophysical flows often consist of transporting vortices as well as time-varying chaotic and nonchaotic regions, just like the double-gyre flow model. Furthermore, at large scales, geophysical flows are often approximated as two-dimensional flows, as the vertical extent of the domain is negligible compared with the surface extent. Thus, the approaches developed here are pertinent to real geophysical flows, and, in fact, could be readily adapted to fully three-dimensional flows.

Although this research provides insights into where to site a single unit for optimal capture capability in a model chaotic flow, the double-gyre flow, the complexity of the broader problem suggests that further research is needed. As Smith *et al.* [16] mentions, it would be worthwhile to consider multiple capture units and how to site them for optimal capture efficiency of the group. Another option is to consider moving capture units, as would be appropriate for removing plastic debris from the ocean or cleaning up oil spills. Other factors such as the effects of particle diffusion could be taken into consideration [73–75]. Furthermore, it is possible to consider localized time dependent sources of tracer particles rather than the uniform initial distribution considered here. In addition, active capture units (for example, the recently opened Orca plant in Iceland for carbon capture) can have high input and output fluxes that alter the local velocity field. How these natural and man-made features affect the interaction between the flow field, the pollutant source(s), and the capture unit(s) suggests several avenues for future work.

ACKNOWLEDGMENT

The authors would like to thank L. D. Smith and I. C. Christov for helpful discussions.

[1] M. Tjahjadi and J. M. Ottino, J. Fluid Mech. **232**, 191 (1991).
[2] G. Lian, C. Thornton, and M. J. Adams, Chem. Eng. Sci. **53**, 3381 (1998).
[3] R. M. Ziff and E. McGrady, J. Phys. A **18**, 3027 (1985).
[4] M. Grzesik and J. Skrzypek, Chem. Eng. Sci. **48**, 2469 (1993).
[5] L. Lebreton, B. Slat, F. Ferrari, B. Sainte-Rose, J. Aitken, R. Marthouse, S. Hajbane, S. Cunsolo, A. Schwarz, A. Levivier *et al.*, Sci. Rep. **8**, 4666 (2018).
[6] Z. Zaman, M. Yu, P. P. Park, J. M. Ottino, R. M. Lueptow, and P. B. Umbanhowar, Nat. Commun. **9**, 3122 (2018).
[7] M. Yu, P. B. Umbanhowar, J. M. Ottino, and R. M. Lueptow, Phys. Rev. E **99**, 062905 (2019).
[8] R. Socolow, M. Desmond, R. Aines, J. Blackstock, O. Bolland, T. Kaarsberg, N. Lewis, M. Mazzotti, A. Pfeffer, K. Sawyer *et al.*, *Direct Air Capture of CO_2 with Chemicals: A Technology Assessment for the APS Panel on Public Affairs*, Technical Report (American Physical Society, New York, 2011).

[9] D. W. Keith, G. Holmes, D. S. Angelo, and K. Heidel, Joule **2**, 1573 (2018).

[10] P. Smith, S. J. Davis, F. Creutzig, S. Fuss, J. Minx, B. Gabrielle, E. Kato, R. B. Jackson, A. Cowie, E. Kriegler *et al.*, Nat. Clim. Change **6**, 42 (2016).

[11] H. Ritchie and M. Roser, Our world in data, https://ourworldindata.org/co2-and-other-greenhouse-gas-emissions (2020).

[12] J. Johnson, C&EN Global Enterprise **97**, 38 (2019).

[13] A. L. Andrady, Mar. Pollut. Bull. **62**, 1596 (2011).

[14] A. Cózar, F. Echevarría, J. I. González-Gordillo, X. Irigoien, B. Úbeda, S. Hernández-León, Á. T. Palma, S. Navarro, J. García-de Lomas, A. Ruiz *et al.*, Proc. Natl. Acad. Sci. USA **111**, 10239 (2014).

[15] W. W. Lau, Y. Shiran, R. M. Bailey, E. Cook, M. R. Stuchtey, J. Koskella, C. A. Velis, L. Godfrey, J. Boucher, M. B. Murphy *et al.*, Science **369**, 1455 (2020).

[16] L. D. Smith, G. Metcalfe, and J. M. Ottino, Phys. Rev. Appl. **10**, 034055 (2018).

[17] F. Lekien, C. Coulliette, A. J. Mariano, E. H. Ryan, L. K. Shay, G. Haller, and J. Marsden, Physica D **210**, 1 (2005).

[18] P. Tallapragada, S. D. Ross, and D. G. Schmale, Chaos **21**, 033122 (2011).

[19] P. J. Nolan, H. G. McClelland, C. A. Woolsey, and S. D. Ross, Sensors **19**, 1607 (2019).

[20] P. J. Nolan, J. Pinto, J. González-Rocha, A. Jensen, C. N. Vezzi, S. C. Bailey, G. De Boer, C. Diehl, R. Laurence, C. W. Powers *et al.*, Sensors **18**, 4448 (2018).

[21] D. G. Schmale and S. D. Ross, Annu. Rev. Phytopathol. **53**, 591 (2015).

[22] S. C. Shadden, F. Lekien, and J. E. Marsden, Physica D **212**, 271 (2005).

[23] C. Coulliette and S. Wiggins, Nonlinear Proc. Geoph. **8**, 69 (2001).

[24] A. C. Poje and G. Haller, J. Phys. Oceanogr. **29**, 1649 (1999).

[25] L. K. Shay, T. M. Cook, H. Peters, A. J. Mariano, R. Weisberg, P. E. An, A. Soloviev, and M. Luther, IEEE J. Oceanic Eng. **27**, 155 (2002).

[26] E. Beckenbach and L. Washburn, J. Geophys. Res. **109**, C2 (2004).

[27] S. C. Shadden, F. Lekien, J. D. Paduan, F. P. Chavez, and J. E. Marsden, Deep Sea Res. II **56**, 161 (2009).

[28] S. Wiggins, *Introduction to Applied Nonlinear Dynamical Systems and Chaos*, Texts in Applied Mathematics Vol. 2 (Springer Science & Business Media, Berlin, 2003).

[29] S. H. Strogatz, *Nonlinear Dynamics and Chaos: With Applications to Physics, Biology, Chemistry, and Engineering* (CRC Press, Boca Raton, FL, 1994).

[30] S. W. Meier, S. E. Cisar, R. M. Lueptow, and J. M. Ottino, Phys. Rev. E **74**, 031310 (2006).

[31] J. M. Ottino, *The Kinematics of Mixing: Stretching, Chaos, and Transport*, Cambridge Texts in Applied Mathematics Series (Cambridge University Press, Cambridge, 1989).

[32] L. D. Smith, P. B. Umbanhowar, J. M. Ottino, and R. M. Lueptow, Phys. Rev. E **96**, 042213 (2017).

[33] A. N. Kolmogorov, Dokl. Akad. Nauk SSSR **98**, 527 (1954).

[34] J. Moser, Matematika **6**, 51 (1962).

[35] V. I. Arnold, Russ. Math. Surv. **18**, 85 (1963).

[36] I. Percival, in *AIP Conference Proceedings*, Vol. 57 (AIP Press, New York, 1980), pp. 302–310.

[37] H. S. Dumas, *The KAM Story: A Friendly Introduction to the Content, History, and Significance of Classical Kolmogorov-Arnold-Moser Theory* (World Scientific, Singapore, 2014).

[38] V. Rom-Kedar, A. Leonard, and S. Wiggins, J. Fluid Mech. **214**, 347 (1990).

[39] R. MacKay, J. Meiss, and I. Percival, Physica D **13**, 55 (1984).

[40] N. Malhotra and S. Wiggins, J. Nonlinear Sci. **8**, 401 (1998).

[41] A. M. Mancho, D. Small, and S. Wiggins, Nonlinear Proc. Geoph. **11**, 17 (2004).

[42] S. Wiggins, Annu. Rev. Fluid Mech. **37**, 295 (2005).

[43] S. Naik, F. Lekien, and S. D. Ross, Regul. Chaotic Dyn. **22**, 272 (2017).

[44] M. A. Stremler, S. D. Ross, P. Grover, and P. Kumar, Phys. Rev. Lett. **106**, 114101 (2011).

[45] P. Grover, S. D. Ross, M. A. Stremler, and P. Kumar, Chaos **22**, 043135 (2012).

[46] W. Bahsoun, C. Bose, and G. Froyland, *Ergodic Theory, Open Dynamics, and Coherent Structures* (Springer, Berlin, 2014).

[47] A. Hadjighasem, M. Farazmand, D. Blazevski, G. Froyland, and G. Haller, Chaos **27**, 053104 (2017).

[48] G. Haller, Chaos **10**, 99 (2000).

[49] G. Haller, Phys. Fluids **13**, 3365 (2001).

[50] G. Haller, Phys. Fluids **14**, 1851 (2002).

[51] G. Haller and G. Yuan, Physica D **147**, 352 (2000).

[52] F. Lekien and S. D. Ross, Chaos **20**, 017505 (2010).

[53] C. Senatore and S. D. Ross, Int. J. Numer. Meth. Eng. **86**, 1163 (2011).

[54] S. G. Raben, S. D. Ross, and P. P. Vlachos, Exp. Fluids **55**, 1638 (2014).

[55] S. G. Raben, S. D. Ross, and P. P. Vlachos, Exp. Fluids **55**, 1824 (2014).

[56] A. E. BozorgMagham, S. D. Ross, and D. G. Schmale, Nonlinear Proc. Geophys. **22**, 663 (2015).

[57] A. E. BozorgMagham and S. D. Ross, Commun. Nonlinear Sci. **22**, 964 (2015).

[58] A. E. BozorgMagham, S. D. Ross, and D. G. Schmale, Physica D **258**, 47 (2013).

[59] P. Tallapragada and S. D. Ross, Commun. Nonlinear Sci. **18**, 1106 (2013).

[60] G. Froyland and K. Padberg, Physica D **238**, 1507 (2009).

[61] G. Froyland, Physica D **200**, 205 (2005).

[62] G. Froyland and M. Dellnitz, SIAM J. Sci. Comput. **24**, 1839 (2003).

[63] G. Froyland, K. Padberg, M. H. England, and A. M. Treguier, Phys. Rev. Lett. **98**, 224503 (2007).

[64] M. Berry, in *American Institute of Physics Conference Proceedings*, Vol. 46 (AIP Press, New York, 1978), p. 16.

[65] R. MacKay and J. Meiss, *Hamiltonian Dynamical Systems* (Institute of Physics, London, 1987).

[66] E. Ott, *Chaos in Dnamical Systems* (Cambridge University Press, Cambridge, 1993).

[67] T. Tél, A. de Moura, C. Grebogi, and G. Károlyi, Phys. Rep. **413**, 91 (2005).

[68] A. Moura, U. Feudel, and E. Gouillart, in *Mixing and Chaos in Open Flows*, Advances in Applied Mechanics Vol. 45 (Elsevier, Amsterdam, 2012), pp. 1–50.

[69] V. I. Arnold and A. Avez, *Ergodic Problems of Classical Mechanics* (W. A. Benjamin, New York, 1968).
[70] I. Mezić, On the geometrical and statistical properties of dynamical systems: Theory and applications, Ph.D. thesis, California Institute of Technology (1994).
[71] I. Mezić and S. Wiggins, Chaos **9**, 213 (1999).
[72] I. Mezić and F. Sotiropoulos, Phys. Fluids **14**, 2235 (2002).
[73] U. Giostra, Aerobiologia **10**, 53 (1994).
[74] C. P. Schlick, I. C. Christov, P. B. Umbanhowar, J. M. Ottino, and R. M. Lueptow, Phys. Fluids **25**, 052102 (2013).
[75] J.-L. Thiffeault and G. A. Pavliotis, Physica D **237**, 918 (2008).